Improved measurement of the $\bar{d}/\bar{u}$ asymmetry in the nucleon sea

R. S. Towell,[1,6] P. L. McGaughey,[6] T. C. Awes,[9] M. E. Beddo,[8] M. L. Brooks,[6] C. N. Brown,[3] J. D. Bush,[1] T. A. Carey,[6] T. H. Chang,[8,*] W. E. Cooper,[3] C. A. Gagliardi,[10] G. T. Garvey,[6] D. F. Geesaman,[2] E. A. Hawker,[10,6] X. C. He,[4] L. D. Isenhower,[1] D. M. Kaplan,[5] S. B. Kaufman,[2] P. N. Kirk,[7] D. D. Koetke,[11] G. Kyle,[8] D. M. Lee,[6] W. M. Lee,[4,†] M. J. Leitch,[6] N. Makins,[2,*] J. M. Moss,[6] B. A. Mueller,[2] P. M. Nord,[11] V. Papavassiliou,[8] B. K. Park,[6] J. C. Peng,[6] G. Petitt,[4] P. E. Reimer,[6,2] M. E. Sadler,[1] W. E. Sondheim,[6] P. W. Stankus,[9] T. N. Thompson,[6] R. E. Tribble,[10] M. A. Vasiliev,[10,‡] Y. C. Wang,[7] Z. F. Wang,[7] J. C. Webb,[8] J. L. Willis,[1] D. K. Wise,[1] and G. R. Young[9]

(FNAL E866/NuSea Collaboration)

[1]*Abilene Christian University, Abilene, Texas 79699*
[2]*Argonne National Laboratory, Argonne, Illinois 60439*
[3]*Fermi National Accelerator Laboratory, Batavia, Illinois 60510*
[4]*Georgia State University, Atlanta, Georgia 30303*
[5]*Illinois Institute of Technology, Chicago, Illinois 60616*
[6]*Los Alamos National Laboratory, Los Alamos, New Mexico 87545*
[7]*Louisiana State University, Baton Rouge, Louisiana 70803*
[8]*New Mexico State University, Las Cruces, New Mexico 88003*
[9]*Oak Ridge National Laboratory, Oak Ridge, Tennessee 37831*
[10]*Texas A & M University, College Station, Texas 77843*
[11]*Valparaiso University, Valparaiso, Indiana 46383*

Measurements of the ratio of Drell-Yan yields from an 800 GeV/c proton beam incident on liquid hydrogen and deuterium targets are reported. Approximately 360 000 Drell-Yan muon pairs remained after all cuts on the data. From these data, the ratio of down antiquark ($\bar{d}$) to up ($\bar{u}$) antiquark distributions in the proton sea is determined over a wide range in Bjorken-x. These results confirm previous measurements by E866 and extend them to lower x. From these data, ($\bar{d}-\bar{u}$) and $\int(\bar{d}-\bar{u})dx$ are evaluated for $0.015 < x < 0.35$. These results are compared with parametrizations of various parton distribution functions, models and experimental results from NA51, NMC and HERMES.

I. INTRODUCTION

Recent measurements [1–4] have shown a large asymmetry in the distributions of up and down antiquarks ($\bar{u}$ and $\bar{d}$) in the nucleon. While no known symmetry requires $\bar{u}$ to equal $\bar{d}$, a large $\bar{d}/\bar{u}$ asymmetry was not anticipated. The usual assumption was that the sea of quark-antiquark pairs is produced perturbatively from gluon splitting. Since the mass difference of the up and down quarks is small, nearly equal numbers of up and down pairs should result. Thus a large $\bar{d}/\bar{u}$ asymmetry requires a non-perturbative origin for this effect.

The data from experiment E866/NuSea [1] at Fermilab were the first to demonstrate a strong Bjorken-x dependence of the $\bar{d}/\bar{u}$ ratio. In that earlier work, only data at fairly large dimuon mass were analyzed. In this paper we report results based on the entire data set and describe the details of the experimental apparatus and analysis procedure. These data cover a larger range of mass and Bjorken-x, and demonstrate

consistency of the results for three different spectrometer settings. They also provide more accurate determinations of $\bar{d}/\bar{u}$, $\bar{d}-\bar{u}$ and the integral of $\bar{d}-\bar{u}$. The data are compared with several parton distribution function sets, and the implications of these results for various models that predict a $\bar{d}/\bar{u}$ asymmetry are discussed.

There have been four other experimental studies [2–5] of the $\bar{d}/\bar{u}$ asymmetry in the nucleon. The first measurement was performed by the New Muon Collaboration (NMC). NMC measured the cross section ratio for deep inelastic scattering (DIS) of muons from hydrogen and deuterium [2]. Their extrapolated result for the integral of the difference of the proton and neutron structure functions is

$$\int_0^1 [F_2^p - F_2^n] \frac{dx}{x} = 0.235 \pm 0.026. \quad (1)$$

This result can be compared with the Gottfried sum rule (GSR) [6]. The Gottfried sum, S_G, can be expressed in terms of the parton distribution functions as

$$S_G \equiv \int_0^1 [F_2^p - F_2^n] \frac{dx}{x} = \frac{1}{3} + \frac{2}{3} \int_0^1 [\bar{u}(x) - \bar{d}(x)] dx. \quad (2)$$

*Present address: University of Illinois at Urbana-Champaign, Urbana, IL 61801.
†Present address: Florida State University, Tallahassee, FL 32306.
‡On leave from Kurchatov Institute, Moscow 123182, Russia.

In the derivation of Eq. (2), charge symmetry was assumed. If it is also assumed that $\int \bar{d}(x)dx = \int \bar{u}(x)dx$, then one arrives at a GSR result of 1/3, in disagreement with the NMC result. Rather, the NMC measurement implies

$$\int_0^1 [\bar{d}(x) - \bar{u}(x)]dx = 0.148 \pm 0.039. \qquad (3)$$

The NMC measurement [2] was the first indication that there are more down antiquarks in the proton than up antiquarks.

In order to obtain the Gottfried sum from the NMC data, an extrapolation was needed to account for contributions to the sum for $x \lesssim 0.004$. Since F_2/x rises rapidly in this region, a sizable contribution to S_G was expected. The small-x extrapolation was checked by Fermilab E665 [7], which made a similar measurement as NMC except that they measured the ratio for $10^{-6} \lesssim x \lesssim 0.3$. Over the kinematic range where NMC and E665 overlap, their measurements agree. However, E665 determined that for $x \lesssim 0.01$ the value of $2F_2^d/F_2^p - 1$ was a constant $0.935 \pm 0.008 \pm 0.034$. While this could be interpreted as a difference between F_2^n and F_2^p, it is usually thought to be the effect of nuclear shadowing in deuterium [8,9] which means that $F_2^n/F_2^p \neq 2F_2^d/F_2^p - 1$. Therefore it is difficult to measure F_2^n/F_2^p in a model-independent way at low x.

Following the publication of the NMC result, it was suggested [10] that the Drell-Yan process [11] could provide a more direct probe of the light antiquark asymmetry of the nucleon. In the parton model, the Drell-Yan cross section at leading order is

$$\frac{d^2\sigma}{dx_1 dx_2} = \frac{4\pi\alpha^2}{9M^2} \sum_i e_i^2 [f_i(x_1)\bar{f}_i(x_2) + \bar{f}_i(x_1)f_i(x_2)], \qquad (4)$$

where the sum is over all quark flavors, e_i are the quark charges, f_i are the parton distribution functions, and M is the virtual photon or dilepton mass [12]. Here x_1 and x_2 are the Bjorken-x of the partons from the beam and target, respectively.

Two kinematic quantities commonly used to describe Drell-Yan events are the Feynman-x (x_F) and the dilepton mass (M) which are defined as

$$x_F = \frac{p_\parallel^\gamma}{p^{\gamma,max}} \approx \frac{p_\parallel^\gamma}{\sqrt{s}/2} = x_1 - x_2 \qquad (5)$$

and

$$M^2 = Q^2 \approx x_1 x_2 s, \qquad (6)$$

where $p_\parallel^\gamma$ is the center-of-mass longitudinal momentum of the virtual photon, $p^{\gamma,max}$ is its maximum possible value, and s is the total four-momentum squared of the initial nucleons. The proton-deuterium Drell-Yan cross section can be expressed as

$$\sigma^{pd} \approx \sigma^{pp} + \sigma^{pn}, \qquad (7)$$

which ignores the small nuclear effects inside the deuterium nucleus. Using this approximation and assuming charge symmetry, the cross section ratio for Drell-Yan events produced in deuterium and hydrogen targets can be used to determine the ratio $\bar{d}/\bar{u}$.

The first experiment to use this idea was the NA51 experiment [3] at CERN. This experiment used the 450 GeV/c proton beam from the CERN Super Proton Synchrotron (SPS) with liquid hydrogen and deuterium targets. The NA51 experiment was able to reconstruct almost 6000 Drell-Yan events with the dimuon mass above 4.3 GeV/c^2, and from these data they obtained

$$\left.\frac{\bar{d}}{\bar{u}}\right|_{\langle x \rangle = 0.18} = 1.96 \pm 0.15 \pm 0.19. \qquad (8)$$

However, the NA51 spectrometer's acceptance was peaked near $x_F = 0$ and $x = 0.18$. This, combined with their limited statistics, made it impossible to determine the x-dependence of the ratio.

Several groups have performed global fits to existing data from DIS, Drell-Yan, and other processes to generate parametrizations of parton distribution functions (PDFs) [13–16]. Prior to the measurements by NMC and NA51 the usual assumption was that $\bar{d}(x) = \bar{u}(x)$. The PDFs were then revised to accommodate the NMC and NA51 data. While these measurements show that $\bar{d} \neq \bar{u}$, neither imposed rigid constraints on the x-dependence of the $\bar{d}(x)/\bar{u}(x)$ asymmetry.

A better measurement of $\bar{d}/\bar{u}$ is possible with Drell-Yan if the detector acceptance is largest for $x_F > 0$, since the Drell-Yan cross section ratio is more sensitive to the target antiquark distribution in this kinematic regime. This increase in sensitivity results from the Drell-Yan cross section being dominated by the annihilation of a beam quark with a target antiquark in this kinematic regime. For $x_1 \gg x_2$, one obtains

$$\sigma^{pp} \propto \frac{4}{9}u(x_1)\bar{u}(x_2) + \frac{1}{9}d(x_1)\bar{d}(x_2) \qquad (9)$$

and

$$\sigma^{pn} \propto \frac{4}{9}u(x_1)\bar{d}(x_2) + \frac{1}{9}d(x_1)\bar{u}(x_2). \qquad (10)$$

From Eqs. (7), (9), and (10) it is a simple matter to derive

$$\left.\frac{\sigma^{pd}}{2\sigma^{pp}}\right|_{x_1 \gg x_2} \approx \frac{1}{2} \frac{\left[1 + \frac{1}{4}\frac{d(x_1)}{u(x_1)}\right]}{\left[1 + \frac{1}{4}\frac{d(x_1)}{u(x_1)}\frac{\bar{d}(x_2)}{\bar{u}(x_2)}\right]} \left[1 + \frac{\bar{d}(x_2)}{\bar{u}(x_2)}\right]. \qquad (11)$$

This expression can be further simplified since $d(x) \ll 4u(x)$, resulting in
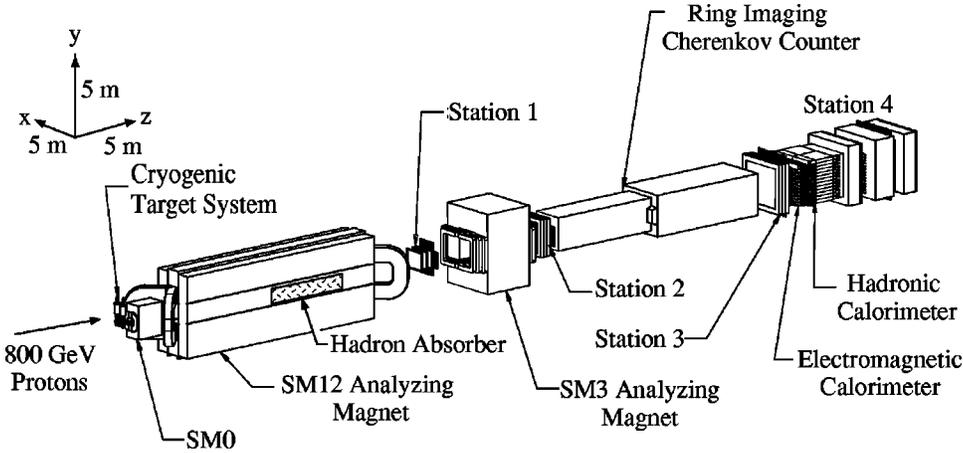
FIG. 1. The FNAL E866/NuSea spectrometer.

$$\frac{\sigma^{pd}}{2\sigma^{pp}}\bigg|_{x_1 \gg x_2} \approx \frac{1}{2}\left[1 + \frac{\bar{d}(x_2)}{\bar{u}(x_2)}\right]. \qquad (12)$$

This equation illustrates the sensitivity of the Drell-Yan cross section ratio to $\bar{d}/\bar{u}$ for $x_1 \gg x_2$.

In Fermilab E866/NuSea [1] the ratio of the Drell-Yan cross section for proton-deuteron interactions to that for proton-proton interactions was measured over a wide range of x and other kinematic variables. This measurement in turn provided an accurate determination of $\bar{d}(x)/\bar{u}(x)$ and an independent determination of the integral of $[\bar{d}(x)-\bar{u}(x)]$ over the same x region.

Recently, the HERMES Collaboration [4] has reported a measurement of $\bar{d}-\bar{u}$ over the range $0.02 < x < 0.30$, based on a measurement of semi-inclusive deep-inelastic scattering. The HERMES results are in good agreement with the results from Fermilab E866/NuSea, but have limited precision.

In Ref. [1], we presented initial results of the Fermilab E866/NuSea study of the light antiquark asymmetry in the nucleon sea, based on an analysis of approximately 40% of our data. Here we present the final results of the analysis of the full data set from the experiment.

II. EXPERIMENTAL SETUP

FNAL E866/NuSea used an 800 GeV/c proton beam extracted from the Fermilab Tevatron accelerator and transported to the east beamline of the Meson experimental hall. The beam position and shape were measured using RF cavities and segmented-wire ionization chambers (SWICs). The final SWIC was located 1.7 m upstream of the target. The beam at this SWIC was typically 6 mm wide and 1 mm high [full width at half maximum (FWHM)]. The most important beam intensity measurement was made with a secondary emission monitor (SEM) located about 100 m upstream of the targets. In addition to the SEM, the beam intensity was monitored with a quarter-wave RF cavity and an ionization chamber. The nominal beam intensity ranged from 5×10^{11} to 2×10^{12} protons per 20 second spill, depending on the spectrometer magnet setting.

The proton beam passed through one of three physically identical, thin, stainless steel target flasks. These flasks were cylindrical in shape with hemispherical ends and insulated vacuum jackets. The flasks were 7.62 cm in diameter and 50.8 cm in length. The two end windows on each flask totaled 0.10 mm of stainless steel and 0.28 mm of titanium. One flask was filled with liquid deuterium, another was filled with liquid hydrogen, and the third was evacuated. The hydrogen target was 7% of an interaction length and 6% of a radiation length, and the deuterium target was 15% of an interaction length and 7% of a radiation length. The evacuated target was less than 0.2% of an interaction length and 1.4% of a radiation length. Both the temperatures and vapor pressures of the filled flasks were monitored.

All three flasks were mounted on a movable table so that the target could be changed during the 40 second gap between the 20 second beam spills. The normal target cycle consisted of twelve spills with five spills on the deuterium target, one spill on the empty flask, five spills on the hydrogen target and another spill on the empty flask. This frequent cycling of the targets minimized many systematic uncertainties.

At 85° to the beam direction there were a pair of four-element scintillator telescopes. These viewed the target through a hole in the heavy shielding enclosing the target area to monitor the luminosity, duty factor, data-acquisition live time, and to independently verify which target was in the beam.

The detector apparatus used in this experiment was the E605 dimuon spectrometer [17], shown in Fig. 1. While changes were made to the spectrometer for E866, the basic design has remained the same since the spectrometer was first used for E605 in the early 1980s. Three large dipole magnets provide for the momentum analysis of energetic muons, while deflecting soft particles out of the acceptance. The magnetic fields are in the horizontal direction, bending the tracks in the vertical direction. The polarities and currents of the first two magnets were adjusted to select particular ranges of dimuon mass, while minimizing background rates in the drift chambers. The changes to the spectrometer for E866 were the installation of six new drift chamber planes at the first tracking station, a reconfigured absorber wall, two new hodoscope planes [18], and a new trigger system [19].

The first dipole magnet (SM0) was used to increase the opening angle of muon pairs when taking data with the magnets configured to have acceptance at the lowest mass. For the higher mass settings it was not energized.

A water-cooled copper beam dump was located at a distance of 1.73 m into the second magnet (SM12). The protons that passed through the target were absorbed in the 3.28-m-long dump. The beam dump was about 22 interaction lengths, or 230 radiation lengths, thick. It filled the magnet aperture in the horizontal direction for most of its length, but was a maximum of 25.4 cm high in the vertical direction. This allowed many of the muons of interest to travel above or below the beam dump, minimizing muon multiple scattering and energy loss.

Downstream of the beam dump was an absorber wall that completely filled the aperture of the magnet. This wall consisted of 0.61 m of copper followed by 2.74 m of carbon and 1.83 m of borated polyethylene. The effect of this wall, which was over thirteen interaction lengths and sixty radiation lengths long, was to absorb most of the produced hadrons, electrons, and gammas. Effectively only muons traversed the active elements of the spectrometer, allowing the use of high beam intensities while keeping the instantaneous number of hits in each drift chamber at an acceptable level.

The third magnet (SM3), located downstream of SM12 and the first tracking station, provided the magnetic field used for the momentum determination of the muons. The position of each muon was measured precisely at three tracking stations, one upstream and two downstream of SM3. Each tracking station consisted of three pairs of high-rate drift chambers, followed by horizontal and vertical scintillation hodoscopes used to generate the dimuon trigger. (The exception to this configuration was the absence of the hodoscope that provides horizontal position information after the second tracking station. This hodoscope was omitted to minimize multiple scattering between the second and third tracking stations.)

At the end of the spectrometer, behind shielding, was the fourth tracking station. It consisted of three planes of proportional tubes and a pair of hodoscope planes. The ring imaging Cherenkov counter (RICH) and two calorimeters, shown in Fig. 1, were not active in E866. The RICH was filled with helium to reduce multiple scattering between the second and third tracking stations. Summaries of the physical construction of the drift chambers, hodoscopes, and proportional tubes may be found in Ref. [18].

III. TRIGGER AND MONITORING

The trigger was optimized to detect dimuon events originating from the target, while rejecting as many muons produced in the beam dump as possible. A new trigger system was implemented for E866 [19,20]. It used the hodoscope signals to determine whether the event should be written to tape. The hits in the hodoscopes at stations 1, 2, and 4 that measured the vertical track positions were compared with the contents of a three-dimensional look-up table. This table was generated by Monte Carlo studies of dimuon events from the target. When the hits in the scintillators matched one of the

TABLE I. Average trigger rates per beam spill and live times for the deuterium target.

Mass setting	Triggers/spill	Live time
low	2200	99.0%
intermediate	3200	97.9%
high	2100	98.5%

pre-calculated dimuon trajectories, the trigger fired.

In addition to the standard physics triggers optimized to detect oppositely charged dimuon events from the targets, other triggers were prescaled to record a limited number of study events. These study events included single-muon events, events satisfying triggers that relied only on the hodoscope planes that provided horizontal position information, and other diagnostic triggers such as two like-sign muons from the target area that traveled down opposite sides (left and right) of the spectrometer.

For each 20 second beam spill, information important for analysis was recorded as part of the data stream. Beam intensity, position, size, and duty factor were recorded, as well as the pressure, temperature, and positions of the liquid targets, magnet voltages and currents, and various monitors used for calculating the readout deadtime. The beam position and size were stable throughout the experiment, well within the dimensions of the target flasks.

To better monitor the spectrometer performance and data quality, a portion of the data was analyzed in real time. The efficiency of each detector element and the overall track reconstruction efficiency were carefully studied. The wire
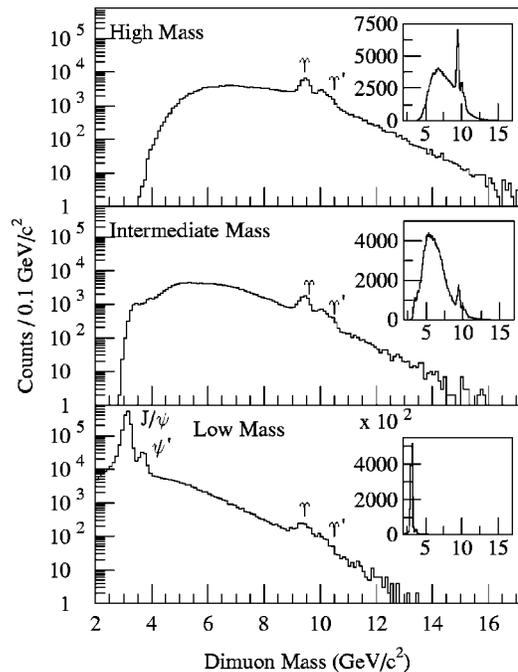
FIG. 2. The dimuon mass distributions for the three different mass settings. The inset figures are the same spectra shown on linear scales. The mass cuts used in the analysis to select Drell-Yan events are listed in Table III.

IMPROVED MEASUREMENT OF THE $\bar{d}/\bar{u}$ ASYMMETRY IN ...

PHYSICAL REVIEW D **64** 052002

chambers had average efficiencies of 96%. The individual hodoscopes used in the trigger were 99% efficient. The overall trigger efficiency was greater than 94%. Average trigger rates and live times for the deuterium target for the three spectrometer settings are given in Table I. Trigger rates were lower and live times higher for the hydrogen target (not shown).

IV. ANALYSIS

The data were taken with three mass settings of the spectrometer magnets, designated as the high, intermediate, and low mass settings. Figure 2 shows the dimuon mass distributions for the three mass settings. The data were further divided based upon the magnet polarity and deuterium target purity. Six data sets contained data useful for this analysis and are summarized in Table II.

A first-pass analysis of the data was done on Fermilab's IBM parallel-computing UNIX farms. Since only about 1% of the events written to tape reconstructed to form a dimuon event from the target, this analysis efficiently reduced the raw data tapes to a small number of data summary tapes (DSTs). After the individual tracks were fully reconstructed, muon pairs were identified. Fewer than 0.08% of all the fully reconstructed events contained more than two muon tracks from the target, resulting in virtually no combinatorial ambiguities.

A second-pass analysis of the DSTs was performed with many small changes to optimize the mass resolution and to study systematic effects. The results were written to PAW ntuples [21] for physics analysis.

Final cuts on the data were carefully studied to assure the removal of bad events, such as interactions outside of the target region. Events were also cut if the reconstructed tracks did not satisfy the trigger conditions. Each beam spill was required to meet certain quality criteria. The beam duty factor, readout live time, and beam intensity were all required to exceed minimum values.

A dimuon mass cut was used to remove the J/ψ and Υ resonance families from the Drell-Yan continuum.[1] The mass regions used for each data set are given in Table III. The number of events remaining in each of the data sets is shown in Table II. Figures 3, 4 and 5 show the resulting dimuon distributions for the three mass settings versus x_1 and x_2.

An important background was the random coincidence of two unrelated, oppositely charged muons. These events are referred to as randoms. The data were corrected for random dimuons by subtracting normalized samples of pairs of combined single muon events from the dimuon sample. The normalization was obtained from the measured yield of like-sign dimuons. The kinematics of the like-sign events were converted to those of opposite-sign pairs by reflecting the vertical angle of one of the tracks, which is equivalent to switching the charge of that muon. There was excellent agreement between the kinematic distributions of these simulated ran-

---

[1]The typical one standard deviation mass resolution at the J/ψ was 100 MeV/c^2 and at the Υ was 150 MeV/c^2.

TABLE II. Summary of the data sets. The size of each set is shown as the number of fully reconstructed Drell-Yan events rounded to the nearest thousand. Magnet p_T kicks are given for SM0 and SM12. SM3 always provided an average p_T kick of 0.9 GeV/c with the same polarity as SM12. All fields are known to $\pm 2\%$. The uncertainties on the deuterium purity are given in Table V.

Mass setting	Drell-Yan events	SM0/SM12 $\langle p_T \text{ kick}\rangle$ [GeV/c]	Deuterium purity
low	89 k	$-1.04/4.72$	99.99%
intermediate	78 k	$0/4.72$	99.99%
intermediate	50 k	$0/-4.72$	99.99%
high	37 k	$0/6.39$	99.99%
high	80 k	$0/6.39$	97.0 %
high	24 k	$0/-6.39$	97.0 %

dom dimuons and the measured like-sign pairs after reflection. Since most of the combined singles events reconstructed to a low effective dimuon mass, the randoms correction was largest in the low-mass data.

The average randoms correction for each mass setting is shown in Table IV. Estimates of single muon rates from J/ψ and semileptonic charm decay, folded with the detector acceptance, are consistent with the observed number of randoms. Another possible background is the dual semileptonic decay of $c\bar{c}$ or $b\bar{b}$ to a correlated $\mu^+\mu^-$. However, both the mass and acceptance for these muon pairs are low, leading to a negligible rate in the Drell-Yan mass regions selected above.

A rate-dependence correction was made for the inefficiency in event detection and reconstruction that occurred as a function of beam intensity. The primary source of this inefficiency is believed to be drift chamber hits lost due to pileup in the single hit TDCs. A decrease in reconstruction efficiency is clearly seen in the low-mass data shown in Fig. 6. The yield of Drell-Yan events per unit beam intensity decreases as the beam intensity increases.

In order to correct the data, the reconstruction efficiency as a function of the beam intensity must be determined. Fits were made to the event yield, normalized by the beam intensity, versus intensity. The data suggest that the reconstruction efficiency drops in a linear manner, and this basic assumption was justified by extensive Monte Carlo simulations. The reconstruction efficiency function was determined independently for each mass setting. The important quantity is not the absolute rate dependence inefficiency, but rather the difference between the inefficiencies for the hydrogen and deu-

TABLE III. Mass regions used for each spectrometer setting for Drell-Yan analysis.

Mass setting	Mass regions accepted
low	4.0 to 8.8 GeV/c^2
intermediate	4.3 to 8.8 GeV/c^2 and >10.8 GeV/c^2
high	4.5 to 9.0 GeV/c^2 and >10.7 GeV/c^2
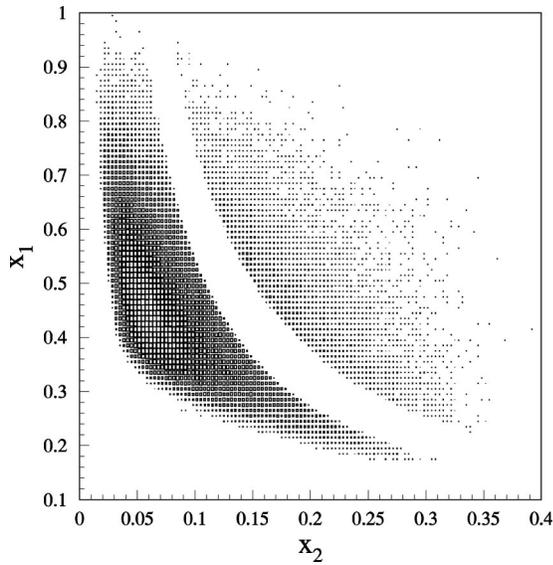
FIG. 3. The dimuon distributions for x_1 versus x_2 for the high mass setting.

FIG. 5. The dimuon distributions for x_1 versus x_2 for the low mass setting.

FIG. 4. The dimuon distributions for x_1 versus x_2 for the intermediate mass setting.

terium targets. The fits to the low mass data are shown in Fig. 6. The final correction to $\sigma^{pd}/2\sigma^{pp}$ due to the rate dependence is given in Table IV. Another concern was that the rate dependence might also be a function of the kinematics of the dimuon event. This dependence was not observed in either the data or Monte Carlo events.

The data included in this analysis were taken over a period of five months. The deuterium target was filled twice during this time. The analysis of the first fill indicated that the deuterium purity was 99.99%. The second fill was of a slightly lesser quality. Table V shows the composition of the second deuterium fill, based on two independent assays. The purity of the liquid hydrogen target was better than 99.99%.

The density of the target material was determined from the vapor pressure of the gas above the liquid in both cryo-genic systems. These pressures were constantly monitored and recorded in a database. The temperature of each flask was also recorded. From these data the average pressure was determined for each target and for each data set. These averaged close to 15 psi. Cryogenic data tables [22] for hydrogen and deuterium were used to convert the vapor pressures to the mass densities shown in Table VI.

The beam was attenuated as it interacted with the target material. Since the deuterium target had the higher density the beam intensity decreased more rapidly as it passed through the deuterium target. Calculations based on the proton-proton and proton-deuteron cross sections [23–26] were used to determine the ratio of the effective luminosity in the hydrogen target, A_h, to the effective luminosity in the deuterium target, A_d:

$$\frac{A_h}{A_d} = 1.042 \pm 0.002. \tag{13}$$

The acceptances for the events from the hydrogen and deuterium targets were not identical. Although the target-flask construction and location were identical, the attenuation of the beam through the targets meant that the average inter-action points for the two targets were slightly different. The average interaction point in the deuterium target was ≈ 0.5 cm upstream of that for the hydrogen target. Monte

TABLE IV. Size of the randoms (background) correction for each mass setting and correction to $\sigma^{pd}/2\sigma^{pp}$ due to the rate-dependence effect.

Mass setting	% random events	$\langle$Mass$\rangle$ (randoms)	Rate correction to $\sigma^{pd}/2\sigma^{pp}$
low	4.1%	4.5 GeV/c^2	5.45% ± 0.82%
intermediate	2.9%	5.1 GeV/c^2	1.06% ± 0.89%
high	0.2%	5.4 GeV/c^2	1.76% ± 0.69%
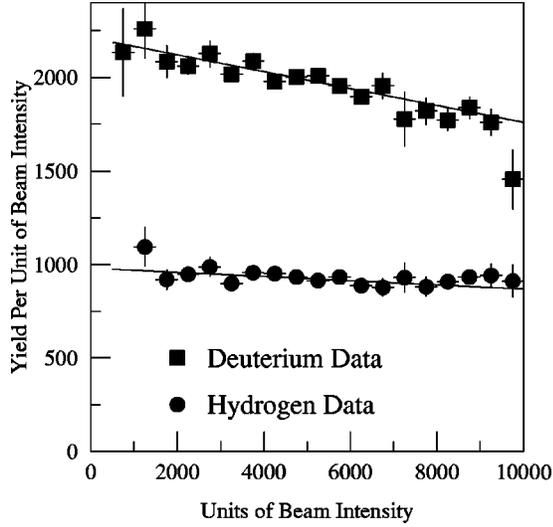
FIG. 6. The rate dependence of the low-mass data. The yield of Drell-Yan events per unit of beam intensity is shown versus the beam intensity for both the hydrogen and deuterium events after corrections due to readout deadtime have been made. The solid lines are a linear fit to the data.

Carlo simulations were done to study the effects of beam attenuation on the acceptance. These studies gave a slight x_2-dependent correction. The maximum size of this correction was about 1% at the highest x_2 data points in the low and intermediate mass data. The typical correction was an order of magnitude smaller.

V. CALCULATION OF $\sigma^{pd}/2\sigma^{pp}$

This experiment counted the number of dimuon events, N, from the hydrogen, deuterium, and empty targets. To compare the yields from these targets, the beam intensity for each spill was recorded and the integrated beam intensity, I, for each target was determined. Using the many small corrections previously described, the number of raw hydrogen dimuon events is

$$N_h = I_h A_h t_h \rho_h \left[\frac{H}{g}\right]\frac{d\sigma^{pp}}{d\Omega}\Delta\Omega_h e_h + N_h^{\mathrm{BG}}, \quad (14)$$

and the number of raw deuterium events is

$$N_d = I_d A_d t_d \rho_d \left[\frac{D}{g}\right]\frac{d\sigma^{pd}}{d\Omega}\Delta\Omega_d e_d + N_d^{\mathrm{BG}}. \quad (15)$$

TABLE V. Composition of the second deuterium fill. The results shown are in percent volume.

Material	Percent volume
D_2	94.05% ± 0.6%
HD	5.90% ± 0.6%
H_2	0.05% ± 0.01%
deuterium	97.0% ± 0.6%
hydrogen	3.0% ± 0.6%

TABLE VI. Average density in g/cm^3 of the liquid targets for each data set.

Mass setting	SM0/SM12 $\langle p_t$ kick$\rangle$ [GeV/c]	Hydrogen (g/cm^3)	Deuterium (g/cm^3)
low	$-1.04/4.72$	0.07066	0.16280
intermediate	$0/4.72$	0.07062	0.16272
intermediate	$0/-4.72$	0.07064	0.16280
high	$0/6.39$	0.07064	0.16278
high	$0/6.39$	0.07062	0.16265
high	$0/-6.39$	0.07061	0.16259

In the equations in this section, the subscripts indicate the target type, hydrogen, h, deuterium, d, and empty, e. The target length is t, H/g and D/g are the number of hydrogen and deuterium atoms per gram, ρ is the target density, $\Delta\Omega$ is the spectrometer acceptance for a given target, e is the detector efficiency for a given target, and N^{BG} is the number of background events for a given target. Using these equations, one obtains

$$\frac{\sigma^{pd}}{2\sigma^{pp}} = \frac{1}{2}\frac{N_d - N_d^{\mathrm{BG}}}{N_h - N_h^{\mathrm{BG}}}\left[\frac{I_h}{I_d}\frac{A_h}{A_d}\frac{t_h}{t_d}\frac{\rho_h}{\rho_d}\frac{H/g}{D/g}\frac{\Delta\Omega_h}{\Delta\Omega_d}\frac{e_h}{e_d}\right]. \quad (16)$$

Note that the quantity in brackets is ≈ 1.

The small amount of hydrogen contamination in the deuterium target after it was filled the second time was accounted for by altering Eq. (15) to read

$$N_d = I_d A_d t_d \rho_d'\frac{D}{g}\left(f_d\frac{d\sigma^{pd}}{d\Omega} + f_h\frac{d\sigma^{pp}}{d\Omega}\right)\Delta\Omega_d e_d + N_d^{\mathrm{BG}}. \quad (17)$$

TABLE VII. Cross section ratios binned in x_2, with their statistical uncertainties and average values for kinematic variables for the high mass data. Systematic uncertainties are reported in Table X.

x_2 range min-max	$\langle x_2\rangle$	$\langle x_F\rangle$	$\langle p_T\rangle$ (GeV/c)	$\langle M_{\mu^+\mu^-}\rangle$ (GeV/c^2)	$\sigma^{pd}/2\sigma^{pp}$
0.015–0.030	0.026	0.624	0.842	5.0	1.029 ± 0.040
0.030–0.045	0.038	0.520	0.935	5.6	1.050 ± 0.018
0.045–0.060	0.053	0.456	1.009	6.3	1.075 ± 0.016
0.060–0.075	0.067	0.411	1.085	6.9	1.107 ± 0.018
0.075–0.090	0.082	0.367	1.133	7.4	1.118 ± 0.020
0.090–0.105	0.097	0.319	1.168	7.8	1.131 ± 0.023
0.105–0.120	0.112	0.279	1.185	8.1	1.150 ± 0.029
0.120–0.135	0.127	0.250	1.202	8.4	1.164 ± 0.034
0.135–0.150	0.142	0.230	1.209	8.8	1.249 ± 0.043
0.150–0.175	0.162	0.213	1.211	9.4	1.105 ± 0.036
0.175–0.200	0.186	0.185	1.206	10.0	1.132 ± 0.047
0.200–0.225	0.212	0.160	1.173	10.7	1.107 ± 0.057
0.225–0.250	0.237	0.128	1.201	11.2	1.028 ± 0.069
0.250–0.300	0.269	0.093	1.180	12.0	0.943 ± 0.071
0.300–0.350	0.315	0.046	1.078	12.9	0.729 ± 0.124

TABLE VIII. Cross section ratios binned in x_2, with their statistical uncertainties and average values for kinematic variables for the intermediate mass data. Systematic uncertainties are reported in Table X.

x_2 range min-max	$\langle x_2 \rangle$	$\langle x_F \rangle$	$\langle p_T \rangle$ (GeV/c)	$\langle M_{\mu^+\mu^-} \rangle$ (GeV/c^2)	$\sigma^{pd}/2\sigma^{pp}$
0.015–0.030	0.027	0.514	1.296	4.6	0.976 ± 0.052
0.030–0.045	0.039	0.386	1.179	4.9	1.050 ± 0.023
0.045–0.060	0.053	0.329	1.152	5.4	1.065 ± 0.018
0.060–0.075	0.067	0.297	1.142	6.0	1.061 ± 0.018
0.075–0.090	0.082	0.265	1.140	6.5	1.118 ± 0.021
0.090–0.105	0.097	0.230	1.144	6.9	1.092 ± 0.023
0.105–0.120	0.112	0.195	1.160	7.1	1.078 ± 0.027
0.120–0.135	0.127	0.161	1.154	7.4	1.152 ± 0.035
0.135–0.150	0.142	0.134	1.118	7.6	1.073 ± 0.038
0.150–0.175	0.161	0.107	1.095	7.9	1.155 ± 0.042
0.175–0.200	0.186	0.081	1.045	8.4	1.164 ± 0.062
0.200–0.225	0.211	0.070	1.080	9.2	1.057 ± 0.082
0.225–0.250	0.234	0.079	1.055	10.3	1.094 ± 0.161
0.250–0.300	0.263	0.153	1.135	12.7	0.868 ± 0.213

In the equation above, f_d and f_h are the percent by volume of deuterium and hydrogen respectively in the deuterium target, and ρ'_d is the density of the contaminated deuterium. The ratio of Drell-Yan cross sections is then

$$\frac{\sigma^{pd}}{2\sigma^{pp}} = \frac{1}{2} \frac{N_d - N_d^{BG}}{N_h - N_h^{BG}} \left[\frac{I_h}{I_d} \frac{A_h}{A_d} \frac{t_h}{t_d} \frac{\rho_h}{f_d \rho'_d} \frac{H/g}{D/g} \frac{\Delta\Omega_h}{\Delta\Omega_d} \frac{e_h}{e_d} \right] - \frac{f_h}{2f_d}. \quad (18)$$

The background events originated from two separate production mechanisms. The first source was Drell-Yan events produced from beam interactions with the target flask windows or other non-target materials. The number of these events was determined by normalizing the yields from the empty target. To properly normalize the number of empty-target events from downstream of the center of the target,

TABLE IX. Cross section ratios binned in x_2, with their statistical uncertainties and average values for kinematic variables for the low mass data. Systematic uncertainties are reported in Table X.

x_2 range min-max	$\langle x_2 \rangle$	$\langle x_F \rangle$	$\langle p_T \rangle$ (GeV/c)	$\langle M_{\mu^+\mu^-} \rangle$ (GeV/c^2)	$\sigma^{pd}/2\sigma^{pp}$
0.015–0.030	0.025	0.495	0.992	4.4	1.064 ± 0.030
0.030–0.045	0.038	0.351	1.036	4.7	1.066 ± 0.018
0.045–0.060	0.052	0.275	1.069	5.0	1.109 ± 0.020
0.060–0.075	0.067	0.238	1.076	5.5	1.092 ± 0.023
0.075–0.090	0.082	0.210	1.065	5.9	1.118 ± 0.029
0.090–0.105	0.097	0.182	1.057	6.3	1.148 ± 0.041
0.105–0.120	0.112	0.151	1.035	6.6	1.138 ± 0.055
0.120–0.135	0.126	0.129	1.051	6.9	1.202 ± 0.093
0.135–0.150	0.141	0.118	1.055	7.4	0.943 ± 0.094
0.150–0.175	0.159	0.091	1.007	7.7	1.039 ± 0.205
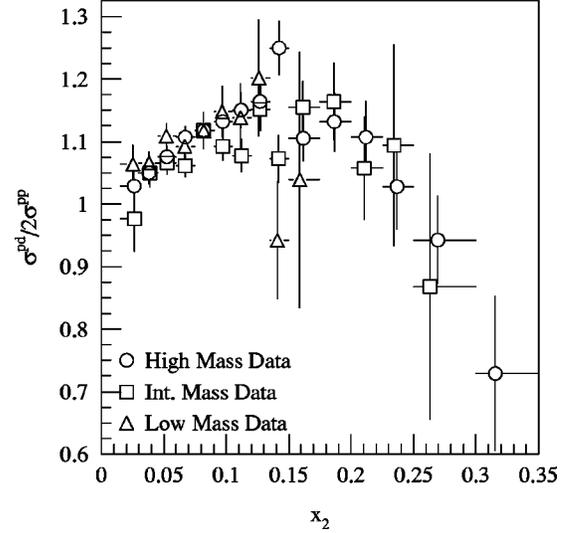
FIG. 7. The Drell-Yan cross section ratio versus x_2. The results from all three mass settings are shown. The error bars represent the statistical uncertainty. The systematic uncertainty is less than 1% for each data set as shown in Table X.

attenuation of the beam through the target must be included. The second source of background events was the randoms ($N_{target}^{randoms}$) that were described previously. Combining these two sources gives

$$N_h^{BG} = (N_e^{up} + 0.93 N_e^{down}) \frac{I_h}{I_e} + N_h^{randoms} \quad (19)$$

for the hydrogen target background and

$$N_d^{BG} = (N_e^{up} + 0.85 N_e^{down}) \frac{I_d}{I_e} + N_d^{randoms} \quad (20)$$

for the deuterium target background. In the previous two equations the superscript on N_e designates whether the empty target event originated from upstream or downstream of the center of the target. Typical empty target corrections are 12% for hydrogen and 5% for deuterium.

The output of the second-pass analysis was subjected to the quality cuts described earlier. Events that passed the cuts, after being corrected for random and non-target events as described above, were used to determine $\sigma^{pd}/2\sigma^{pp}$ versus x_2. These results are shown in Tables VII, VIII, and IX. The

TABLE X. Systematic uncertainties in the measurement of $\sigma^{pd}/2\sigma^{pp}$.

Source of uncertainty	Mass setting		
	High	Intermediate	Low
rate dependence	0.69%	0.89%	0.82%
target length	0.2 %	0.2 %	0.2 %
beam intensity	0.1 %	0.1 %	0.1 %
attenuation and acceptance	0.2 %	0.2 %	0.2 %
deuterium composition	0.61%		
total	0.97%	0.94%	0.87%
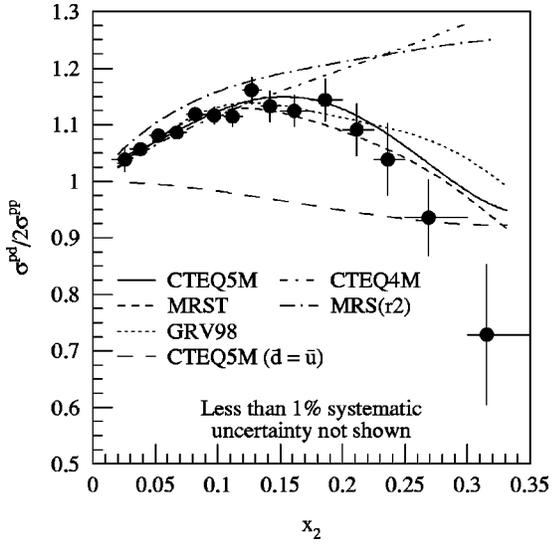
FIG. 8. The Drell-Yan cross section ratio versus x_2. The results from all three mass settings have been combined. The error bars represent the statistical uncertainty. The systematic uncertainty is common to all points and is less than 1%. The curves are the calculated next-to-leading-order cross-section ratios using various parton distribution functions. The bottom curve is calculated using CTEQ5M where $\bar{d}-\bar{u}$ has been forced to zero.

results shown for the high-mass data are slightly different from and supersede those previously published [1], due to minor improvements made to the rate dependence and acceptance calculations. These improvements changed the relative normalization between the hydrogen and deuterium targets by $\sim 0.6\%$, well within the systematic uncertainty of 0.97%. The average values of x_2, x_F, p_T, and dimuon mass are also shown in Tables VII, VIII, and IX.

The average cross-section ratios for each mass setting are shown in Fig. 7. The three mass settings agree and are consistent within their systematic uncertainties. (see also Table X). The result of averaging all of the mass settings is shown in Fig. 8 and Table XI.

Since this is a measurement of cross-section ratios, the only sources of systematic uncertainty that must be considered are those that affect the two targets differently. Because the targets were changed every few minutes, effects such as changes in detector efficiency or beam quality were minimized.

The important sources of systematic uncertainty include differences in the rate dependence, target flask length, target composition, beam attenuation, and acceptance. Table X shows the main sources of systematic uncertainty in the cross section ratio for each mass setting. Clearly the rate dependence and deuterium composition are the dominant uncertainties. Adding all of the sources of systematic uncertainties in quadrature, the total systematic uncertainty in the measured cross section ratio is less than 1%.

VI. EXTRACTION OF $\bar{d}(x)/\bar{u}(x)$

From the discussion in Sec. I, it is clear that $\sigma^{pd}/2\sigma^{pp}$ is closely related to $\bar{d}/\bar{u}$. However, the simple approximations

that lead to Eq. (12) are not fully satisfied since the data cover a larger range in x_F. Therefore, an iterative process was used to extract $\bar{d}/\bar{u}$ versus x_2 from the cross-section ratio.

The iterative process calculated $\sigma^{pd}/2\sigma^{pp}$ at leading order,[2] folded it with the experimental acceptance, and compared this calculated quantity with the measurement. Next, the $\bar{d}/\bar{u}$ ratio was adjusted to improve the agreement. This process continued until the calculated $\sigma^{pd}/2\sigma^{pp}$ agreed with the measured ratio. The results of this method, using the combined data from all mass settings, are shown in Fig. 9 together with parametrizations from various PDFs [13,14,27–29].

It is clear from Eq. (4) that the calculation of $\sigma^{pd}/2\sigma^{pp}$ requires the PDF for each quark and antiquark in the proton as input. In the iterative process, it was assumed that existing PDF parametrizations accurately describe the valence and heavy-quark distributions as well as the quantity $\bar{d}(x) + \bar{u}(x)$, since these quantities have been constrained by previous measurements. The parametrizations used were CTEQ5M [27] and those of Martin, Roberts, Stirling and Thorne (MRST) [28].

For $\sigma^{pd}/2\sigma^{pp}$ calculated from the PDFs to be compared to the measured $\sigma^{pd}/2\sigma^{pp}$, the acceptance of the spectrometer must be included. To do this the cross section ratio was calculated for the x_1, x_2, and Q^2 values of every real event that passed the analysis cuts. These calculated cross section ratios were then averaged over each x_2 bin.

As $\sigma^{pd}/2\sigma^{pp}$ was calculated for each iteration, it was assumed that $\bar{d}/\bar{u}$ for the beam proton was the same as $\bar{d}/\bar{u}$ for the target proton over the x_2 range of the data. For many events however, x_1 was greater than the maximum x_2 in the data, so some assumption was required for the value of $\bar{d}(x_1)/\bar{u}(x_1)$ for $x_1 \gtrsim 0.35$. The effects of several different assumptions were investigated. The extracted $\bar{d}/\bar{u}$ was not noticeably affected by any of these assumptions except at the highest x values, where $\bar{d}/\bar{u}$ was affected by less than five percent. The assumption finally used was $\bar{d}(x_1)/\bar{u}(x_1) \equiv 1.0$ in the proton for $x_1 > 0.35$.

Once the quantity $\bar{d}(x)/\bar{u}(x)$ was determined, the quantity $\bar{d}(x) - \bar{u}(x)$ was calculated, again assuming that the quantity $\bar{d}(x) + \bar{u}(x)$ is well described by the parametrizations. So that $\bar{d}(x) - \bar{u}(x)$ could be integrated, the $\bar{d}(x)/\bar{u}(x)$ values were scaled to a fixed Q^2, with $Q = 7.35$ GeV/c. The scaling procedure multiplied $\bar{d}(x,Q)/\bar{u}(x,Q)$ by the ratio $[\bar{d}(x,Q=7.35)/\bar{u}(x,Q=7.35)]/[\bar{d}(x,Q)/\bar{u}(x,Q)]$ as given by CTEQ5M. (There was no significant difference if MRST was used instead of CTEQ5M.) Figure 10 and Table XI show $\bar{d}(x) - \bar{u}(x)$ as a function of x. These data can be integrated over x to provide $\int_0^1 [\bar{d}(x) - \bar{u}(x)]dx = 0.118 \pm 0.012$ for the

---

[2] The difference between next-to-leading-order and leading-order calculations of the cross section *ratio* in the region of interest is less than 2.1%.

TABLE XI. The cross section ratio, $\bar{d}/\bar{u}$ and $\bar{d}-\bar{u}$ values determined from the combination of all data sets for each x_2 bin. The first uncertainty is statistical and the second uncertainty is systematic. The quantities extracted from the cross section ratio are given for $Q^2 = 54$ GeV$^2/c^2$. The cross section ratio has a systematic uncertainty of less than 1% as shown in Table X. The average values for kinematic variables are also shown.

x_2 range min-max	$\langle x_2 \rangle$	$\langle x_F \rangle$	$\langle p_T \rangle$ (GeV/c)	$\langle M_{\mu^+\mu^-} \rangle$ (GeV/c^2)	$\sigma^{pd}/2\sigma^{pp}$	$\bar{d}/\bar{u}$	$\bar{d}-\bar{u}$
0.015–0.030	0.026	0.534	1.004	4.6	1.038 ± 0.022	$1.085 \pm 0.050 \pm 0.017$	$0.862 \pm 0.489 \pm 0.167$
0.030–0.045	0.038	0.415	1.045	5.1	1.056 ± 0.011	$1.140 \pm 0.027 \pm 0.018$	$0.779 \pm 0.142 \pm 0.096$
0.045–0.060	0.052	0.356	1.076	5.6	1.081 ± 0.010	$1.215 \pm 0.026 \pm 0.020$	$0.711 \pm 0.077 \pm 0.060$
0.060–0.075	0.067	0.326	1.103	6.2	1.086 ± 0.011	$1.249 \pm 0.028 \pm 0.021$	$0.538 \pm 0.055 \pm 0.041$
0.075–0.090	0.082	0.296	1.122	6.8	1.118 ± 0.013	$1.355 \pm 0.036 \pm 0.023$	$0.512 \pm 0.044 \pm 0.028$
0.090–0.105	0.097	0.261	1.141	7.2	1.116 ± 0.015	$1.385 \pm 0.046 \pm 0.025$	$0.400 \pm 0.040 \pm 0.022$
0.105–0.120	0.112	0.227	1.156	7.5	1.115 ± 0.018	$1.419 \pm 0.060 \pm 0.027$	$0.321 \pm 0.038 \pm 0.017$
0.120–0.135	0.127	0.199	1.168	7.8	1.161 ± 0.023	$1.630 \pm 0.085 \pm 0.031$	$0.338 \pm 0.034 \pm 0.013$
0.135–0.150	0.142	0.182	1.161	8.2	1.132 ± 0.027	$1.625 \pm 0.110 \pm 0.033$	$0.259 \pm 0.035 \pm 0.010$
0.150–0.175	0.161	0.164	1.156	8.7	1.124 ± 0.027	$1.585 \pm 0.111 \pm 0.032$	$0.180 \pm 0.027 \pm 0.008$
0.175–0.200	0.186	0.146	1.146	9.5	1.144 ± 0.038	$1.709 \pm 0.158 \pm 0.036$	$0.142 \pm 0.023 \pm 0.005$
0.200–0.225	0.211	0.133	1.146	10.3	1.091 ± 0.047	$1.560 \pm 0.194 \pm 0.034$	$0.081 \pm 0.022 \pm 0.004$
0.225–0.250	0.236	0.120	1.178	11.1	1.039 ± 0.063	$1.419 \pm 0.264 \pm 0.036$	$0.045 \pm 0.023 \pm 0.003$
0.250–0.300	0.269	0.097	1.177	12.0	0.935 ± 0.067	$1.082 \pm 0.256 \pm 0.032$	$0.006 \pm 0.019 \pm 0.002$
0.300–0.350	0.315	0.046	1.078	12.9	0.729 ± 0.124	$0.346 \pm 0.395 \pm 0.022$	$-0.040 \pm 0.036 \pm 0.002$

proton. An extrapolation was made to account for the unmeasured region at low x. To extrapolate this integral from the measured region, which is shown in Fig. 11, to the unmeasured region, MRST and CTEQ5M were used to estimate the contribution for $0 \leqslant x \leqslant 0.015$ and it was assumed that the contribution for $x \geqslant 0.35$ was negligible. The uncertainty from this extrapolation was estimated to be 0.0041 which is half the difference between the contributions as given by MRST and CTEQ5M.
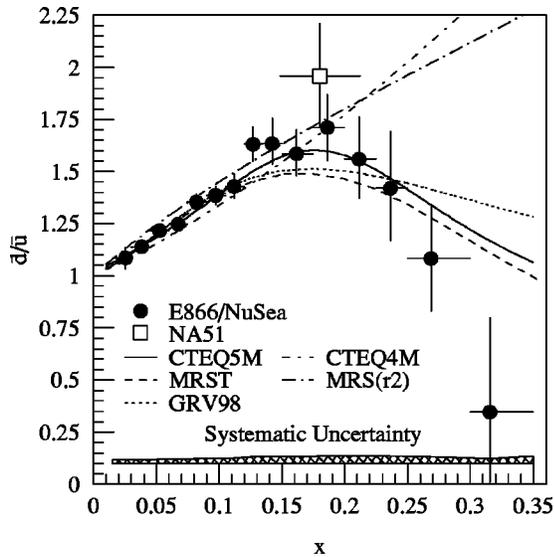
FIG. 9. $\bar{d}(x)/\bar{u}(x)$ versus x shown with statistical and systematic uncertainties. The combined result from all three mass settings is shown with various parametrizations. The E866 data and the parametrizations are at $Q^2 = 54$ GeV$^2/c^2$. The NA51 data point is also shown.

VII. CHARGE SYMMETRY AND SHADOWING

The analysis presented here assumes that the parton distributions of the nucleon obey charge symmetry: i.e., $u_p(x) = d_n(x)$, $\bar{d}_p(x) = \bar{u}_n(x)$, etc. This is consistent with the treatment in previous experiments [1–4] and global fits [13–15]. The possibility that charge symmetry could be significantly
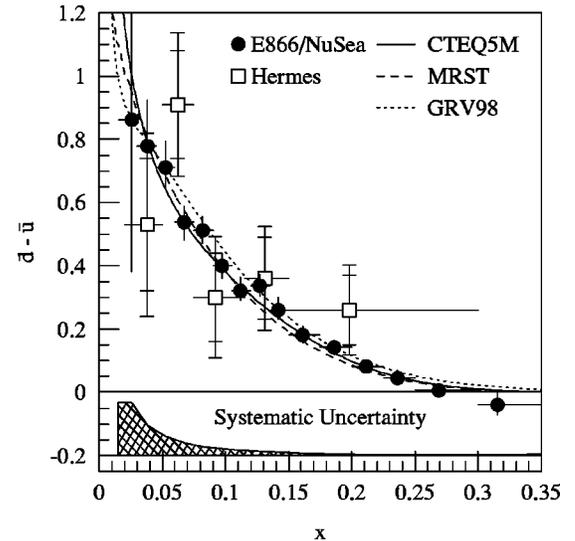
FIG. 10. $\bar{d}-\bar{u}$ as a function of x shown with statistical and systematic uncertainties. The E866 results, scaled to fixed $Q^2 = 54$ GeV$^2/c^2$, are shown as the circles. Results from HERMES ($\langle Q^2 \rangle = 2.3$ GeV$^2/c^2$) are shown as squares. The error bars on the E866 data points represent the statistical uncertainty. The inner error bars on the HERMES data points represent the statistical uncertainty while the outer error bars represent the statistical and systematic uncertainty added in quadrature.
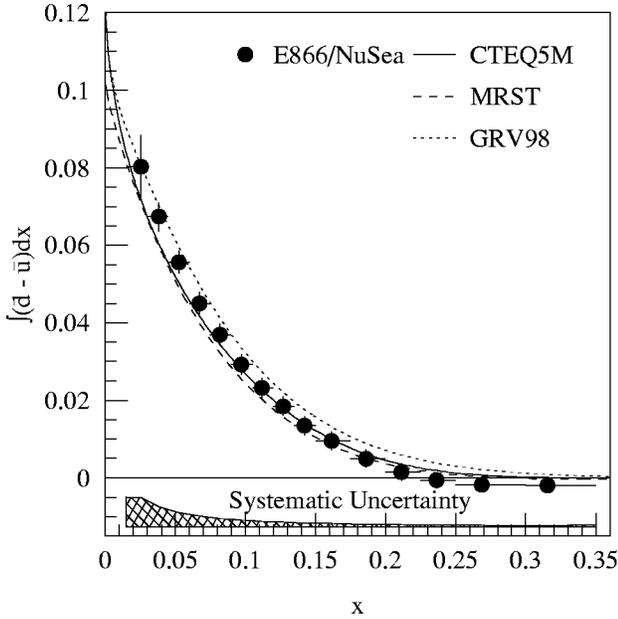
FIG. 11. $\int_x^{0.35}[\bar{d}(x') - \bar{u}(x')]dx'$ versus x shown with statistical and systematic uncertainties at fixed $Q^2 = 54$ GeV$^2/c^2$. The curves are from three different parametrizations.

FIG. 12. The Drell-Yan cross section ratio versus p_T. The combined result from all data sets is shown. The error bars represent the statistical uncertainty. There is a one percent systematic uncertainty common to all points.

violated (CSV) at the parton level has been discussed by several authors [30–36] and an extensive review was recently published [36].

Using the cloudy-bag model, it has been demonstrated [33] that a CSV effect of $\approx 5\%$ could exist for the "minority valence quarks" [i.e., $d_p(x)$ and $u_n(x)$] at $x > 0.4$. In contrast, a study [35] of sea quark CSV showed it to be roughly a factor of 10 smaller than CSV for valence quarks. This was called into question in an analysis by Boros *et al.* [37,38] of the F_2 structure functions determined from muon and neutrino deep inelastic scattering, which concluded that $\bar{d}_n(x) \approx 1.25\bar{u}_p(x)$ at small x. However, Bodek *et al.* [39] showed that W charge asymmetry measurements are inconsistent with the CSV effect identified by Boros *et al.* and consistent with the assumption of sea quark charge symmetry. Subsequently, a more recent work by Boros *et al.* [40] concluded that, after corrections are made for nuclear shadowing in the neutrino-induced data and the charm production threshold is treated explicitly using next leading order (NLO) QCD, the deep inelastic muon and neutrino scattering data provide no evidence for sea quark CSV.

Throughout the above analysis, we have assumed that nuclear effects in deuterium may be neglected, so that $\sigma^{pd} = \sigma^{pp} + \sigma^{pn}$. This is consistent with the traditional approach, in which nuclear effects in deuterium are included in global parton distribution fits [27–29] and neglected in experimental analyses [1–4]. However, it is important to estimate the magnitude of these corrections. The nuclear dependence of proton-induced Drell-Yan dimuon production at 800 GeV/c has been determined by Fermilab E866/NuSea [41] and by Fermilab E772 [42]. These experiments measured the relative Drell-Yan cross sections per nucleon on a range of nuclear targets. Both experiments find little, if any, nuclear dependence for $x > 0.08$. In this region, we may conserva-

tively estimate that any nuclear effects in the proton-deuterium Drell-Yan cross section are $< 0.5\%$. However, at small x, the nuclear data show clear evidence for nuclear shadowing. In principle, one may use the parametrization $\sigma^{pA} = \sigma_0 A^\alpha$, where A is the atomic number, to extrapolate the observed effects in heavier nuclei to deuterium. But this will overestimate them, due to the anomalously large inter-nucleon separation in the deuteron.
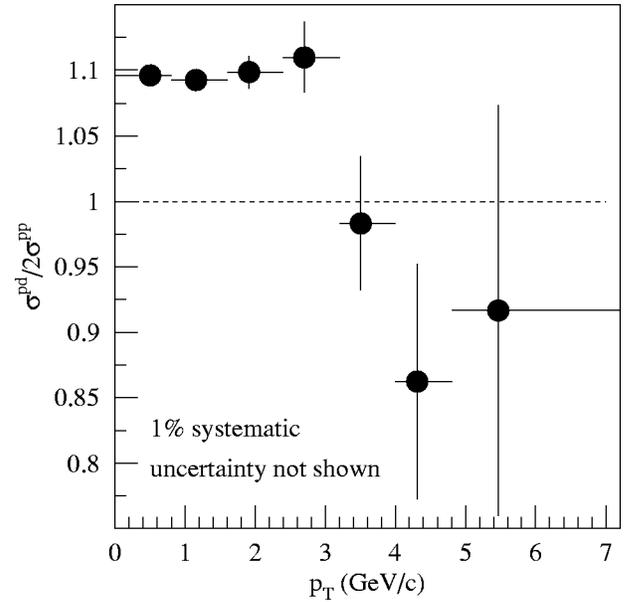
Alternatively, one may note that the shadowing effects seen in Drell-Yan by E866 [41] and in deep inelastic scattering by NMC [43] are nearly equal, in spite of the different reaction mechanisms and momentum transfers of the two experiments, so we may use calculations of shadowing in deep inelastic scattering [8,9] to set the scale of the nuclear effects that may be present in our deuterium data. We estimate that shadowing implies a reduction of 0.9% to σ^{pd} in Eq. (7) for our smallest x_2 point, based on the calculations of Badelek and Kwiecinski [9]. This would increase $\bar{d}(x)/\bar{u}(x)$ by $< 2\%$ in our x range. Our extracted value of $(\bar{d} - \bar{u})|_{x=0.026}$ would increase by 26%. The correction to $\bar{d} - \bar{u}$ drops very rapidly as x increases. Our value for $\int_{0.015}^{0.35}(\bar{d} - \bar{u})dx$ would increase by 10%. The nuclear effects in deuterium, and hence the corrections to our results, are estimated to be approximately half as large in the calculations of Melnitchouk and Thomas [8]. We conclude that the correction due to shadowing in deuterium may be comparable to our systematic uncertainty for our smallest x values, and is much smaller than our systematic uncertainty for $x > 0.06$.

VIII. DEPENDENCE ON OTHER KINEMATIC VARIABLES

The cross section ratio for deuterium versus hydrogen can be studied as a function of kinematic quantities other than

TABLE XII. $\int[\bar{d}(x)-\bar{u}(x)]dx$ evaluated over different x ranges based on three parametrizations and as measured by E866 ($Q^2 = 54$ GeV$^2/c^2$).

x range	CTEQ5M	MRST	GRV98	E866
$0<x<1$	0.1255	0.1149	0.1376	0.118 ± 0.012
$0.35<x<1$	-0.0001	-0.0003	0.0004	
$0.015<x<0.35$	0.0837	0.0815	0.0897	0.0803 ± 0.011
$0<x<0.015$	0.0418	0.0337	0.0475	

x_2. Figure 12 shows the ratio as a function of the transverse momentum of the dimuon. Studies of the data and of Monte Carlo acceptance calculations show that the observed shape versus p_T is not due to acceptance differences between the targets or correlations with x_2.

For p_T values below 3 GeV/c there may be evidence for a slight rise in the ratio with p_T, consistent with a small amount of additional multiple scattering of the incoming parton in deuterium. Above 3 GeV/c the ratio drops abruptly to near or below unity. This could be a signature for a change in reaction mechanism.

Recently, Berger *et al.* [44] calculated the p_T dependence of the Drell-Yan cross section off an (isoscalar) nucleon to $O(\alpha_s^2)$, including the modifications at small p_T due to all-orders soft-gluon resummation. They find that the quark-antiquark annihilation process $q\bar{q}\rightarrow\gamma^*X$ dominates the Drell-Yan yield at small p_T, and the quark-gluon Compton scattering process $qg\rightarrow q\gamma^*X$ dominates at large p_T. This implies that the sensitivity of $\sigma^{pd}/2\sigma^{pp}$ to $\bar{d}/\bar{u}$ arises primarily at small p_T, while the large-p_T ratio measures the relative gluon densities in the proton and deuteron. The calculations indicate that the crossover between the two processes occurs at $p_T\sim 2$ to 3 GeV/c for the kinematics of the E866 data, close to the point where the cross-section ratio versus p_T in Fig. 12 begins to drop. Thus, the E866 $\sigma^{pd}/2\sigma^{pp}$ results may also provide information regarding the gluonic composition of the nucleon, but such an analysis is outside the scope of the present paper.

The dependences of the deuterium to hydrogen ratio on x_1, x_F, and dimuon mass were also studied. Unlike p_T, these studies showed no independent dependence on these kinematic variables, reinforcing the conclusion that x_2 is the important variable for our data.

IX. COMPARISON TO OTHER RESULTS

The results of this experiment are much more extensive and precise than any other measurement of $\bar{d}(x)/\bar{u}(x)$. Other

TABLE XIII. $\int[\bar{d}(x)-\bar{u}(x)]dx$ as determined by three experiments. The range of the measurement is shown along with the value of the integral over all x.

Experiment	x range	$\int_0^1[\bar{d}(x)-\bar{u}(x)]dx$
E866	$0.015<x<0.35$	0.118 ± 0.012
NMC	$0.004<x<0.80$	0.148 ± 0.039
HERMES	$0.020<x<0.30$	0.16 ± 0.03

measurements of $\bar{d}(x)/\bar{u}(x)$ include the early measurement by NA51 and the recent result from the HERMES collaboration at DESY. These measurements are in general agreement with the E866 results as seen in Fig. 9 and Fig. 10. Even though the average Q^2 values of these measurements differ, comparisons can be made between them because the Q^2 dependence is small.

While the NA51 determination of $\bar{d}(x)/\bar{u}(x)$ was very similar to the method used by E866, the HERMES result was based on a measurement of semi-inclusive deep-inelastic scattering. The HERMES data have neither the coverage nor the precision of E866, but provide a truly independent confirmation of the results. Many of the systematic effects that are common to the NA51 and E866 Drell-Yan experiments do not affect the HERMES measurement.

These measurements of $\bar{d}(x)/\bar{u}(x)$ can be compared to the NMC DIS results by integrating $\bar{d}(x)-\bar{u}(x)$. Table XII summarizes the value of this integral over various x ranges as parametrized by three global fits and as measured by E866. Table XIII summarizes three experimental determinations of this integral over all x values. The E866 integral is smaller than those from NMC and HERMES, but consistent with them within the quoted uncertainties.

X. STRUCTURE OF THE NUCLEON SEA

Ever since evidence for a flavor-asymmetric sea was reported by NMC and NA51, the groups performing global analysis for PDFs have required $\bar{d}$ to be different from $\bar{u}$. The NMC result constrains the integral of $\bar{d}-\bar{u}$ to be 0.148 ±0.039, while the NA51 result requires $\bar{d}/\bar{u}$ to be 1.96 ±0.25 at $x=0.18$. Clearly, the x-dependences of $\bar{d}-\bar{u}$ and $\bar{d}/\bar{u}$ were undetermined. Recently, several PDF groups have published [27–29] new parametrizations taking into account new experimental results, including the E866 data reported in Ref. [1]. The parametrizations of the x dependences of $\bar{d}-\bar{u}$ are now strongly constrained by E866. As shown in Fig. 9, these new parametrizations give significantly different shapes for $\bar{d}/\bar{u}$ at $x>0.15$ compared to previous works such as CTEQ4M and MRS(r2).

It is interesting to note that the E866 data also affect the parametrization of the valence-quark distributions. Figure 13 shows the NMC data for $F_2^p-F_2^n$ at $Q^2=4$ GeV$^2/c^2$, together with the fits of MRS(r2) and MRST. It is instructive to decompose $F_2^p(x)-F_2^n(x)$ into contributions from valence and sea quarks:

$$F_2^p(x)-F_2^n(x)=\frac{1}{3}x[u_v(x)-d_v(x)]+\frac{2}{3}x[\bar{u}(x)-\bar{d}(x)].$$

(21)

As shown in Fig. 13, the E866 data provide a direct determination of the sea-quark contribution to $F_2^p-F_2^n$. (The original E866 results from Ref. [1] are shown, rather than the more precise results reported here, because they were used as inputs for the MRST PDF fits.) In order to preserve the fit to $F_2^p-F_2^n$, the MRST parametrization for the valence-quark
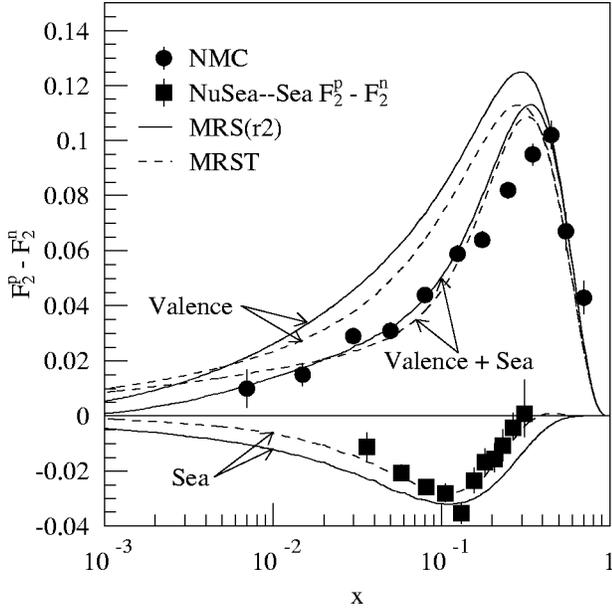
FIG. 13. $F_2^p - F_2^n$ as measured by NMC at $Q^2 = 4$ GeV$^2/c^2$ compared with next-to-leading-order calculations based on the MRS(r2) and MRST parametrizations. Also shown are the original E866 results from Ref. [1], scaled to $Q^2 = 4$ GeV$^2/c^2$, for the sea-quark contribution to $F_2^p - F_2^n$. For each parametrization, the top (bottom) curve is the valence (sea) contribution and the middle curve is the sum of the two.

FIG. 14. $F_2^p - F_2^n$ as measured by NMC at $Q^2 = 4$ GeV$^2/c^2$ compared with the parametrization of MRST. The dashed curve corresponds to $0.21x^{0.62}$, a parametrization assumed by NMC for the unmeasured small-x region when the Gottfried integral was evaluated.

distributions, $u_v - d_v$, is significantly lower in the region $x > 0.01$ than MRS(r2). Indeed, one of the major new features of MRST is that d_v is now significantly larger than before for $x > 0.01$. Although the authors of MRST attribute this to the new W-asymmetry data from CDF and the new NMC results on F_2^n/F_2^p, it appears that the new information on $\bar{d}(x) - \bar{u}(x)$ also has a direct impact on the valence-quark distributions.

Another implication of the E866 data is on the behavior of $F_2^p - F_2^n$ at small x. In order to satisfy the constraint $\int_0^1 [u_v(x) - d_v(x)]dx = 1$, the MRST values of $u_v(x) - d_v(x)$ at $x < 0.01$ are now much larger than in previous PDFs. This is because the MRST parametrization of $u_v(x) - d_v(x)$ at $x > 0.01$ is smaller than before. As a consequence, $F_2^p - F_2^n$ is increased at small x and MRST predicts a large contribution to the Gottfried sum from the small-x ($x < 0.004$) region, as shown in Fig. 14. If the MRST parametrization for $F_2^p - F_2^n$ at $x < 0.004$ were used together with the NMC data at $x > 0.004$, one would deduce a larger value for the Gottfried sum, and a value for the $\bar{d} - \bar{u}$ integral smaller than that of Eq. (3). This would bring better agreement between the E866 and the NMC results on the $\bar{d} - \bar{u}$ integral.

XI. ORIGINS OF THE NUCLEON SEA

The Fermilab E866/NuSea results for $\bar{d}(x)/\bar{u}(x)$ and $\bar{d}(x) - \bar{u}(x)$ provide important constraints on models that attempt to describe the origins of the nucleon sea and its anti-

quark asymmetry. The early assumption of flavor symmetry in the nucleon sea presumed that the primary mechanism to generate the sea is gluon splitting into $u\bar{u}$ and $d\bar{d}$ pairs. Field and Feynman [45] suggested that the extra valence u quark in the proton could lead to a suppression of $g \to u\bar{u}$ relative to $g \to d\bar{d}$ via Pauli blocking. Ross and Sachrajda [46] subsequently calculated that the effects of Pauli blocking are very small, and more recent calculations [47] have confirmed this result, even indicating that the overall effect of Pauli blocking may have the opposite effect to naive expectations. Given the small mass difference between the u and d quarks, we are left with the conclusion that perturbative QCD is incapable of generating a $\bar{d}/\bar{u}$ asymmetry of the magnitude observed by E866. Thus, this effect must have a non-perturbative origin. As these nonperturbative mechanisms are considered, it is important to remember that they act in addition to the perturbative sources, which tends to dilute their effect. In effect the non-perturbative sources must be even stronger to account for the large asymmetries shown here. Several models have been proposed, including meson-cloud contributions, chiral-field or chiral-soliton effects, and instantons. Figure 15 compares the E866 results for $\bar{d}(x) - \bar{u}(x)$ to predictions of representative models of each of these types.

The coupling of the nucleon to virtual states containing isovector mesons provides a natural mechanism to produce a $\bar{d}/\bar{u}$ asymmetry. For example, the valence quarks present in the πN component of the proton have $\bar{d}/\bar{u} = 5$. Since Thomas pointed out their importance [48], many authors have investigated virtual meson-baryon Fock states of the nucleon as the origin of the $\bar{d}/\bar{u}$ asymmetry in the sea. Two recent
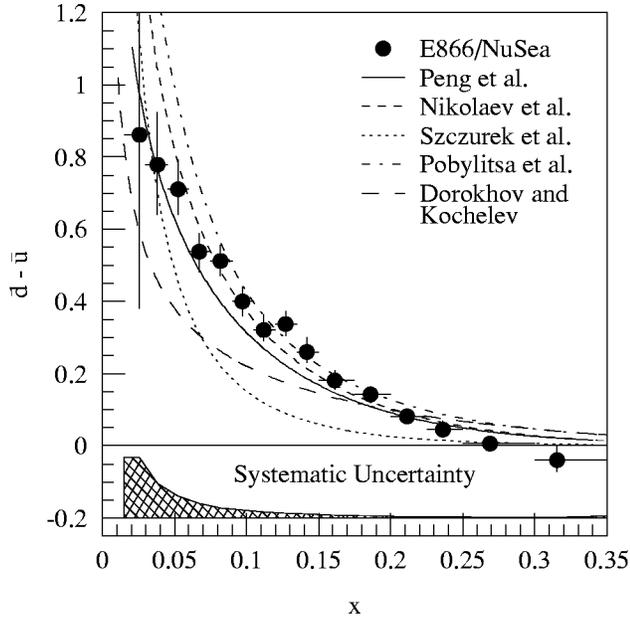
FIG. 15. Comparison of the measured $\bar{d}(x) - \bar{u}(x)$ at $Q^2 = 54$ GeV^2/c^2 to predictions of several models of the nucleon sea. The solid and short-dash curves show pion-cloud calculations by Peng *et al.* and Nikolaev *et al.*, respectively. The dotted curve shows the chiral perturbation theory calculation of Szczurek *et al.*, while the dot-dash curve shows the chiral quark-soliton calculation of Pobylitsa *et al.* The long-dash curve shows the instanton model prediction of Dorokhov and Kochelev.

reviews [49,50] provide a detailed survey of the literature.

Most calculations include contributions from πN and $\pi \Delta$ configurations. $g_{\pi NN}$ and $g_{\pi N\Delta}$ are the well known pion-nucleon and pion-delta coupling constants, so the primary difference among the various calculations is the treatment of the πNN and $\pi N\Delta$ vertex form factors. As an example, Fig. 15 compares the present determination of $\bar{d}(x) - \bar{u}(x)$ to a pion-cloud-model calculation [51], which followed a procedure detailed by Kumano [52]. In this calculation, dipole form factors were used, with $\Lambda = 1.0$ GeV for the πNN vertex and $\Lambda = 0.8$ GeV for the $\pi N\Delta$ vertex. This calculation is typical of many of this type, in that the probability of finding the nucleon in a πN configuration is approximately twice that of finding it in the $\pi \Delta$ configuration [53,54]. However, a recent calculation by Nikolaev *et al.* [55], also shown in Fig. 15, calls this into question. After isolating the contribution to inclusive particle production from Reggeon exchange, they conclude that the $\pi N\Delta$ vertex should be substantially softer than previously believed, significantly reducing the probability of finding the nucleon in a $\pi \Delta$ configuration. It adopts Gaussian form factors with cutoff parameters of 1 GeV^{-2} for the πNN vertex and 2 GeV^{-2} for the $\pi N\Delta$ vertex. This calculation predicts that the πN component of the nucleon is slightly more probable than in Ref. [51] and the $\pi \Delta$ component is very small. Thus, while it provides very good agreement with the E866 results for $x > 0.05$, it contains significantly more singular behavior as $x \to 0$. Overall, it predicts that

$$\int_0^1 [\bar{d}(x) - \bar{u}(x)] dx = 0.177. \tag{22}$$

While the pion-cloud calculations above give a good description of the measured $\bar{d}(x) - \bar{u}(x)$, they are not able to predict $\bar{d}(x)/\bar{u}(x)$ since neither one attempts to describe the entire light antiquark sea. Rather, they assume that an additional symmetric contribution exists due to gluon splitting to bring the $\bar{d}/\bar{u}$ ratio down to the measured value. These models do however indicate that pions make up a large part of the sea where the asymmetry is greatest. In contrast, Alberg *et al.* [56] have investigated whether or not the entire light antiquark sea might be understood in a meson-cloud picture. They find that, by considering πN and ωN contributions, they can fit $\bar{d}(x) - \bar{u}(x)$ and simultaneously obtain a reasonable description of $\bar{d}/\bar{u}$ at $x < 0.25$. They also speculate that the addition of $\pi \Delta$, ρN and σN terms would preserve the fit to $\bar{d} - \bar{u}$, because of a cancellation between the $\pi \Delta$ and ρN effects, and further improve the agreement for $\bar{d}/\bar{u}$.

A different approach to the $\bar{d}/\bar{u}$ asymmetry, based on chiral perturbation theory, has been proposed by Eichten *et al.* [57]. Within their model, the asymmetry arises from the coupling of constituent quarks to Goldstone bosons, such as $u \to d\pi^+$ and $d \to u\pi^-$. The excess of $\bar{d}$ over $\bar{u}$ is then simply due to the additional valence u quark in the proton. Figure 15 includes the result of such a calculation, based on a calculation of $\bar{d}(x) - \bar{u}(x)$ at $Q_0 = 0.5$ GeV/c by Szczurek *et al.* [58], and evolved to $Q^2 = 54$ GeV^2/c^2. It clearly predicts too soft an asymmetry. This arises because the model treats the three valence quarks equivalently at the initial scale, with each carrying 1/4 of the nucleon momentum. (Gluons carry the remaining 1/4.) The $\bar{d}/\bar{u}$ ratio is then fixed by Clebsch-Gordan coefficients to be 11/7 for all x at Q_0. With this input, QCD evolution requires $\bar{d}/\bar{u} \lesssim 11/7$, independent of x and Q. Hence, unlike the meson-baryon models, this model underpredicts $\bar{d}/\bar{u}$ over much of the measured x range. E866 results suggest that additional correlations between the chiral constituents of the nucleon need to be taken into account. The chiral quark-soliton model has been used by Pobylitsa *et al.* [59] to calculate $\bar{d}(x) - \bar{u}(x)$ in the large-N_c limit. Figure 15 shows that this model reproduces the measured $\bar{d}(x) - \bar{u}(x)$ values well for $x > 0.08$, but it overestimates the asymmetry at small x.

The spin and flavor structure of the nucleon sea have been investigated in the instanton model by Dorokhov and Kochelev [60]. They derive expressions for the x dependence of the instanton-induced sea that are appropriate for very large and very small x. They then combine the two asymptotic forms to obtain an *ad hoc* expression for all x,

$$\bar{d}_I(x) - \bar{u}_I(x) = 1.5 A \frac{(1-x)^7}{x \ln^2 x}, \tag{23}$$

where A is an arbitrary constant which they chose to reproduce early NMC results. This form gives a poor description

of our measured $\bar{d}(x) - \bar{u}(x)$, as shown in Fig. 15, where we have set $A = 0.163$ to give $\int_0^1 (\bar{d} - \bar{u}) dx = 0.118$. The model also predicts that instanton-induced antiquarks should arise primarily at large p_T ($\langle p_T^2 \rangle \approx 2$ GeV$^2/c^2$), but Fig. 12 shows that the asymmetry we have measured is not primarily a high-p_T effect. Finally, the model predicts that $\bar{d}/\bar{u} \to 4$ as $x \to 1$ for the instanton-induced component of the nucleon sea. Clearly, the experimental results strongly contradict this, so this model would require a large additional contribution to the sea from $g \to q\bar{q}$ as $x \to 1$ to bring $\bar{d}/\bar{u}$ into agreement. We do not know if an alternative formulation of the instanton model, especially including a more realistic treatment of the momentum dependence at finite x, might provide a better description of our results.

XII. CONCLUSIONS

While previous experiments have indicated that $\bar{d} > \bar{u}$, FNAL E866/NuSea was the first measurement of the x-dependence of the flavor asymmetry in the nucleon sea. This measurement has had an impact in several areas. The global parametrizations of the nucleon sea have changed to fit these new data. Surprisingly, this measurement, when used in conjunction with the NMC measurement, puts new and tighter constraints on the valence PDFs. This measurement has also provided a means of testing the predictions of several nonperturbative models [51]. The unexpected sharp downturn in $\bar{d}(x)/\bar{u}(x)$ apparently back to unity at the large x limits of this measurement has prompted interest [61] in extending the measurement of $\sigma^{pd}/2\sigma^{pp}$ to higher x. An experiment has been proposed [62] to make this measurement using the 120 GeV/c proton beam from the new Main Injector at Fermilab.

The primary goal of this experiment was the determination of $\sigma^{pd}/2\sigma^{pp}$ over a wide kinematic range. The combined result from all three mass settings is shown in Fig. 8 along with the curves from the calculated cross section ratio using various parametrizations. Parametrizations that do not include the first published results [1] from this experiment do not agree well with the data. From the complete set of data, $\bar{d}(x)/\bar{u}(x)$, $\bar{d}(x) - \bar{u}(x)$, and $\int [\bar{d}(x) - \bar{u}(x)] dx$ of the proton were determined. These are shown in Figs. 9, 10, and 11. Models that explicitly include pions in the proton wave function [51] are relatively successful at reproducing the observed flavor asymmetry.

ACKNOWLEDGMENTS

---

[1] Fermilab E866/NuSea Collaboration, E.A. Hawker *et al.*, Phys. Rev. Lett. **80**, 3715 (1998).

[2] New Muon Collaboration, P. Amaudruz *et al.*, Phys. Rev. Lett. **66**, 2712 (1991); M. Arneodo *et al.*, Phys. Rev. D **50**, R1 (1994).

[3] NA51 Collaboration, A. Baldit *et al.*, Phys. Lett. B **332**, 244 (1994).

[4] HERMES Collaboration, K. Ackerstaff *et al.*, Phys. Rev. Lett. **81**, 5519 (1998).

[5] E772 Collaboration, P.L. McGaughey *et al.*, Phys. Rev. Lett. **69**, 1726 (1992).

[6] K. Gottfried, Phys. Rev. Lett. **18**, 1174 (1967).

[7] E665 Collaboration, M.R. Adams *et al.*, Phys. Rev. Lett. **75**, 1466 (1995).

[8] W. Melnitchouk and A.W. Thomas, Phys. Rev. D **47**, 3783 (1993).

[9] B. Badelek and J. Kwiecinski, Phys. Rev. D **50**, R4 (1994).

[10] S.D. Ellis and W.J. Stirling, Phys. Lett. B **256**, 258 (1991).

[11] S.D. Drell and T.M. Yan, Phys. Rev. Lett. **25**, 316 (1970).

[12] C. Grosso-Pilcher and M.J. Shochet, Annu. Rev. Nucl. Part. Sci. **36**, 1 (1986).

[13] H.L. Lai *et al.*, Phys. Rev. D **55**, 1280 (1997).

[14] A.D. Martin, R.G. Roberts, and W.J. Stirling, Phys. Lett. B **387**, 419 (1996).

[15] M. Glück, E. Reya, and A. Vogt, Z. Phys. C **67**, 433 (1995).

[16] H. Plothow-Besch, Int. J. Mod. Phys. A **10**, 2901 (1995); Comput. Phys. Commun. **75**, 396 (1993).

[17] E605 Collaboration, G. Moreno *et al.*, Phys. Rev. D **43**, 2815 (1991).

[18] R.S. Towell, Ph.D. thesis, University of Texas, 1999, nucl-ex/0102012.

[19] C.A. Gagliardi *et al.*, Nucl. Instrum. Methods Phys. Res. A **418**, 322 (1998).

[20] E. A. Hawker, Ph.D. thesis, Texas A&M University, 1998.

[21] R. Bock *et al.*, Comput. Phys. Commun. **45**, 181 (1987).

[22] H. M. Roder, G. E. Childs, R. D. McCarty, and P. E. Angerhofer, *Survey of the Properties of the Hydrogen Isotopes Below their Critical Temperatures*, National Bureau of Standards Technical Note 641 (1973).

[23] T.J. Roberts *et al.*, Nucl. Phys. **B159**, 56 (1979).

[24] A.S. Carroll *et al.*, Phys. Lett. **80B**, 319 (1979).

[25] A.S. Carroll *et al.*, Phys. Lett. **61B**, 303 (1976).

[26] A. Breakstone *et al.*, Nucl. Phys. **B248**, 253 (1984).

[27] H.L. Lai *et al.*, Eur. Phys. J. C **12**, 375 (2000).

[28] A.D. Martin, R.G. Roberts, W.J. Stirling, and R.S. Thorne, Eur. Phys. J. C **4**, 463 (1998).

[29] M. Glück, E. Reya, and A. Vogt, Eur. Phys. J. C **5**, 461 (1998).

[30] B. Ma, Phys. Lett. B **274**, 111 (1992).

[31] B. Ma, A. Schäfer, and W. Greiner, Phys. Rev. D **47**, 51 (1993).

[32] E. Sather, Phys. Lett. B **274**, 433 (1992).

[33] E.N. Rodionov, A.W. Thomas, and J.T. Londergan, Mod. Phys. Lett. A **9**, 1799 (1994).

[34] C.J. Benesh and T. Goldman, Phys. Rev. C **55**, 441 (1997).

[35] C.J. Benesh and J.T. Londergan, Phys. Rev. C **58**, 1218 (1998).

[36] J.T. Londergan and A.W. Thomas, Prog. Part. Nucl. Phys. **41**, 49 (1998).

[37] C. Boros, J.T. Londergan, and A.W. Thomas, Phys. Rev. Lett. **81**, 4075 (1998).

[38] C.l Boros, J.T. Londergan, and A.W. Thomas, Phys. Rev. D **59**, 074021 (1999).

[39] A. Bodek, Q. Fan, M. Lancaster, K.S. McFarland, and U.K. Yang, Phys. Rev. Lett. **83**, 2892 (1999).

[40] C. Boros, F.M. Steffens, J.T. Londergan, and A.W. Thomas, Phys. Lett. B **468**, 161 (1999).

[41] FNAL E866/NuSea Collaboration, M.A. Vasiliev *et al.*, Phys. Rev. Lett. **83**, 2304 (1999).

[42] D.M. Alde *et al.*, Phys. Rev. Lett. **64**, 2479 (1990).

[43] New Muon Collaboration, M. Arneodo *et al.*, Nucl. Phys. **B481**, 3 (1996); **B481**, 23 (1996).

[44] E.L. Berger, L.E. Gordon, and M. Klasen, Phys. Rev. D **58**, 074012 (1998).

[45] R.D. Field and R.P. Feynman, Phys. Rev. D **15**, 2590 (1977).

[46] D.A. Ross and C.T. Sachrajda, Nucl. Phys. **B149**, 497 (1979).

[47] F.M. Steffens and A.W. Thomas, Phys. Rev. C **55**, 900 (1997).

[48] A.W. Thomas, Phys. Lett. **126B**, 97 (1983).

[49] S. Kumano, Phys. Rep. **303**, 183 (1998).

[50] J.P. Speth and A.W. Thomas, Adv. Nucl. Phys. **24**, 83 (1997).

[51] Fermilab E866/NuSea Collaboration, J.C. Peng *et al.*, Phys. Rev. D **58**, 092004 (1998).

[52] S. Kumano, Phys. Rev. D **43**, 59 (1991); **43**, 3067 (1991); S. Kumano and J.T. Londergan, *ibid.* **44**, 717 (1991).

[53] A. Szczurek, J. Speth, and G.T. Garvey, Nucl. Phys. **A570**, 765 (1994).

[54] W. Koepf, L.L. Frankfurt, and M. Strikman, Phys. Rev. D **53**, 2586 (1996).

[55] N.N. Nikolaev, W. Schäfer, A. Szczurek, and J. Speth, Phys. Rev. D **60**, 014004 (1999).

[56] M. Alberg, E.M. Henley, and G.A. Miller, Phys. Lett. B **471**, 396 (2000).

[57] E.J. Eichten, I. Hinchliffe, and C. Quigg, Phys. Rev. D **45**, 2269 (1992); **47**, R747 (1993).

[58] A. Szczurek, A. Buchmans, and A. Faessler, J. Phys. G **22**, 1741 (1996).

[59] P.V. Pobylitsa, M.V. Polyakov, K. Goeke, T. Watabe, and C. Weiss, Phys. Rev. D **59**, 034024 (1999).

[60] A.E. Dorokhov and N.I. Kochelev, Phys. Lett. B **259**, 335 (1991); **304**, 167 (1993).

[61] W. Melnitchouk, J. Speth, and A.W. Thomas, Phys. Rev. D **59**, 014033 (1999).

[62] P906 Collaboration, D. F. Geesaman *et al.*, Fermi National Accelerator Laboratory Proposal 906, 1999.